Published online 20 December 2012 *Nucleic Acids Research, 2013, Vol. 41, No. 3* ***1569–1580***
doi:10.1093/nar/gks1270

Effect of capsid confinement on the chromatin organization of the SV40 minichromosome

Gadiel Saper[1,2], Stanislav Kler[3], Roi Asor[1], Ariella Oppenheim[3,*], Uri Raviv[1,*] and Daniel Harries[1,2,*]

[1]Institute of Chemistry, The Hebrew University, Jerusalem 91904, Israel, [2]The Fritz Haber Research Center, The Hebrew University, Jerusalem 91904, Israel and [3]Department of Hematology, Hebrew University–Hadassa Medical School, Jerusalem 91120, Israel

Received July 5, 2012; Revised October 26, 2012; Accepted November 5, 2012

ABSTRACT

Using small-angle X-ray scattering, we determined the three-dimensional packing architecture of the minichromosome confined within the SV40 virus. In solution, the minichromosome, composed of closed circular dsDNA complexed in nucleosomes, was shown to be structurally similar to cellular chromatin. In contrast, we find a unique organization of the nanometrically encapsidated chromatin, whereby minichromosomal density is somewhat higher at the center of the capsid and decreases towards the walls. This organization is in excellent agreement with a coarse-grained computer model, accounting for tethered nucleosomal interactions under viral capsid confinement. With analogy to confined liquid crystals, but contrary to the solenoid structure of cellular chromatin, our simulations indicate that the nucleosomes within the capsid lack orientational order. Nucleosomes in the layer adjacent to the capsid wall, however, align with the boundary, thereby inducing a 'molten droplet' state of the chromatin. These findings indicate that nucleosomal interactions suffice to predict the genome organization in polyomavirus capsids and underscore the adaptable nature of the eukaryotic chromatin architecture to nanoscale confinement.

INTRODUCTION

The formation of viruses from proteins and nucleic acids is a striking example of complex self assembly. Many viruses form icosahedral, almost spherical capsids, inside which nucleic acid is packaged. Bacteriophages, for example, package linear double-stranded DNA (dsDNA) using motor proteins, thereby achieving dense, highly ordered and pressurized DNA organization (1–7). Other viruses package linear single-stranded RNA (ssDNA) through direct electrostatic interactions between RNA and capsid protein that nucleate capsid assembly (8–10). These viruses typically show high density of RNA lining the interior of the viral capsid (11–14).

The genome of simian virus 40 (SV40), a non-enveloped icosahedral virus and member of the polyomaviridae (15), poses additional constraints to packaging. The viral genome is a 5.2-kb circular dsDNA, wrapped around histone octamers, forming a chromatin-like structure with ~20 nucleosomes, termed the 'minichromosome' (16–18). Unlike cellular chromatin or minichromosomes isolated during the infection cycle (18), minichromosomes packaged within the mature virion lack histone H1 proteins, most likely facilitating condensation. The viral capsid surrounding the viral chromatin comprises three viral-encoded proteins VP1, VP2 and VP3. In total, 72 VP1 pentamers arrange in a $T = 7$ icosahedral lattice with ~50-nm external diameter and ~36-nm internal diameter (19,20). Long, flexible carboxy-terminal arms tie the pentamers together in three different types of interactions, allowing gaps between the subunits.

During assembly, capsomers are added around the minichromosome (21) leading to its compaction. In this process, the minichromosome must overcome the frustration arising from internucleosomal (predominantly steric) interactions, as well as confinement by the capsid walls. The three-dimentional, higher-order structure of the closed circular minichromosme within the capsid of polyomaviruses (as well as papillomaviruses) confined inside this nanometric-sized cavity remains unknown. In contrast, *cellular* chromatin is known to be present as ~10-nm fiber in 'beads on string' or 'open', transcriptionally active structure, or alternatively as ~30 nm 'closed', often inactive fiber configuration. Although the *in vivo* prevalence and relevance of the

*To whom correspondence should be addressed. Tel: +972 2 6585484; Fax: +972 2 6513742; Email: daniel.harries@mail.huji.ac.il
Correspondence may also be addressed to Ariella Oppenheim. Tel: +972 2 6776753; Fax: +972 2 6423067; Email: ariella.oppenheim@mail.huji.ac.il
Correspondence may also be addressed to Uri Raviv. Tel: +972 2 6586030; Fax: +972 2 5618033; Email: Uri.Raviv@mail.huji.ac.il

30-nm chromatin fiber is still under debate (22,23), a number of different higher-order structures for this configuration have been suggested by several authors, including solenoid, zigzag, superbead, and other architectures (24–30). The uncertainty in structure appears to be related to the particular nature of the nucleosome arrays studied, and to the sensitivity of the 30-nm fiber to changes in external conditions, witnessed both experimentally and by high-resolution and coarse-grained simulations [see ref (30) for a recent extensive review]. Interestingly, once released from the virion, the SV40 minichromosome assumes chromatin structures reminiscent of cellular chromatin, which depends on pH (18) and salt concentration (17).

An early theoretical model of the packaged minichromosome based on volume restrictions (31) concluded that the chromatin may fit into the capsid with little configurational freedom. While at that time the precise shape and size of the nucleosome and capsid volume were ambiguous, the model highlighted the strong nucleosomal confinement within the SV40 capsid.

Dubochet and co-workers attempted to capture the packaged minichromosome structure by rapidly vitrifying samples following lysis of virion particles (32). However, once the minichromosome was released from the confines of the virions, the minichromosome quickly assumed a different structure. Freshly prepared minichromosomes (containing 20–25 nucleosomes) at close to physiological ionic strength (130 mM NaCl) were found condensed into globules, 30 nm in size or more. At low ionic strength (<10 mM NaCl), the minichromosomes opened, first into 10 nm filaments and then into nucleosome-strings. The globule-like structure was explained by a liquid drop model, whereby nucleosomes assemble through stacking interaction to form distorted (solenoid, 30 nm) or fragmented 10-nm filaments. These structures cannot represent the tight sphere-like confinement of the packaged minichromosome, yet are consistent with the interactions in solution of nucleosomal core particles (NCPs), as demonstrated by detailed experiments (33,34).

NCPs result from digestion of inter-nucleosomal linker DNA and can be approximated as discs of 5 nm height and 10 nm diameter (35). Depending on their concentration and on solution parameters, such as pH and osmotic pressure (exerted by PEG polymer) (33,34), NCPs show complex phase behavior in solution, and can assemble into well-defined macroscopic liquid crystalline order (36). For example, similar to phases found for discotic or oblate ellipsoids that are favored by steric packing considerations (37), NCPs at densities found inside the virus, and at physiological conditions, form columnar or even higher-order phases (36,38). Under physiological salt concentration (~150 mM), NCPs show net attraction, as determined by osmotic pressure measurements that yield the so-called second virial coefficient (33). This attraction may further facilitate the formation of condensed columnar phases (36).

To gain insight into the interplay between minichromosome confinement and molecular interactions, we used a combination of solution small-angle X-ray scattering (SAXS) experiments and coarse-grained computational modeling. Our results suggest that, when averaged over a large ensemble of viruses, the SV40 minichromosome within the virion adopts configurations consisting of somewhat higher chromatin density in the center and lower mean densities for larger radii. Good agreement between simulations and experiments allows us to rationalize the forces and interactions leading to the observed organization, and to predict structural features that have not yet been resolved by experiments. Importantly, we find that weak, non-specific and steric interactions are sufficient to account for the minichromosomal structure within the SV40 capsid.

MATERIALS AND METHODS

Preparation of wt SV40, empty capsid and DNA-VLPs

SV40 stocks were prepared as previously described (39) and separated into full (DNA-containing) and empty particles as detailed in *SI sec.1a*. Virus-like particles (VLPs), containing dsDNA (DNA-VLPs), were prepared as previously described (40,41) and detailed in *SI sec.1b*.

SAXS

The methodology followed for measuring the diffraction of viral particles has been previously described (42,43) and is detailed in *SI sec.1c*.

To model the SV40 samples, a form factor of multiple concentric spherical shells with smoothly varying electron density (ED) profiles, represented by hyperbolic tangent functions:

$$\Delta\rho(\mathrm{r}) = 0.5\left\{\Delta\rho_1 + \sum_{i=1}^{N-1}[(\Delta\rho_{i+1} - \Delta\rho_i)]\tanh[s_i(r - R_i)]\right\} \quad (1)$$

was fit to the data, as described (42,43). $\Delta\rho(r)$ indicates the radial ED contrast with respect to the solvent (buffer). The index i represents the ith layer in the sphere, with an outer radius, R_i, an ED contrast, $\Delta\rho_i$, and linked to the subsequent layer $(i+1)$ by a slope s_i. $\Delta\rho_N = 0$ and corresponds to the solvent ED contrast. To numerically solve arbitrary ED profiles, the form factor of the smooth ED profiles, $\Delta\rho(r)$ were calculated by discretizing the profiles and transforming them to a sum of Heaviside step functions that can be analytically solved (42,43).

An improved fit ($T = 7$ model) to the scattering data from wtSV40 was obtained by replacing the protein capsid layer (the third layer in Table 1) with spheres of smoothly varying ED contrast (Equation 1 with N = 2), located at the center of each pentamer, represented by:

$$\Delta\rho(\vec{r}) = \sum_{i=0}^{N} 0.5\left\{\Delta\rho_{Core,1} + \sum_{\mathrm{i}=1}^{\mathrm{N}-1}\left[(\Delta\rho_{Core,i+1} - \Delta\rho_{Core,i})\right] \times \tanh\left[\mathrm{s_i}\left(|\vec{r}| - R_i\right)\right]\right\} + 0.5\left\{\Delta\rho_{Capsid} - \Delta\rho_{Capsid} \times \tanh\left[S_{Capsid}\left(|\vec{r}| - a\right)\right]\right\} \otimes \sum_{n=1}^{72}\delta(\vec{r} - f \times \vec{R}_n) \quad (2)$$

The first term in the expression represents the ED profile inside the capsid as a sum of multiple concentric spherical shells as described in Equation 1. The second term

Table 1. Parameters for the best fit models of the SAXS data (presented in Figure 1a–c) for wt SV40, empty capsids and VLP (DNA-VLPs)

Model parameter	wt SV40	Empty capsid	DNA-VLPs
[b]R_1 [nm]	9.2	16.0	16.7
[a]$\Delta\rho_1$ (ρ_1) (e/nm^3)	40 (373)	13 (346)	2 (335)
s_1 (nm^{-1})	0.2	0.3	0.4
[b]R_2 (nm)	18.1	24.4	24.9
[a]$\Delta\rho_2$ (ρ_2) (e/nm^3)	37 (370)	43 (376)	55 (388)
s_2 (nm^{-1})	0.7	7.2	1.6
[b]R_3 (nm)	24.4		
[a]$\Delta\rho_3$ (ρ_3) (e/nm^3)	49 (382)		
s_3 (nm^{-1})	0.5		
Background	$0.0739q^{-2.43}+0.0343$	$0.076q^{-2.84}+0.566q^{-0.36}$	$0.417q^{-1.96}+0.031$

[a]The error in the ED is ±2.
[b]The error in the radii is ±0.1 nm.

represents the arrangement of the 72 VP1 pentamers in the capsid shell. This term results from a convolution between a sphere, with an outer radius a and ED $\Delta\rho_{\text{Capsid}}$, and a sum of delta functions shifted by a set of vectors $f\times\vec{R}_n$. The $\vec{R}_n$ vectors represent the locations of the center of mass of the 72 VP1 pentamers derived from the crystal structure of wtSV40 (20). The fitting parameter f enables us to change the radius of the particle.

Monte carlo simulations

Using the Metropolis algorithm (44), we performed Monte Carlo simulations in the canonical (NVT) ensemble, whereby nucleosomes were modeled as oblate ellipsoids confined within a spherical shell, as parameterized by experiments and further detailed in *SI sec.1d-g*, Supplementary Figures S1–S4.

The attractive potential between the nucleosomes is known to be determined by the salt concentration in solution. In our simulations, we assume that the 1:1 salt concentration in solution is set by the parameter λ that, more generally, represents the Lagrange multiplier associated with constraints set by solution conditions. This parameter is used in the standard metropolis algorithm to determine transition probabilities as

$$P(a\rightarrow b)=\begin{cases}1, & E_b\le E_a\\ e^{-(E_b-Ea)/\lambda k_BT}, & E_b>E_a\end{cases} \quad (3)$$

Where $P(a\rightarrow b)$ is the transition probability at any step from a state with energy E_a to a state with energy E_b.

Variation in λ in the simulations leads to a modulation of effective forces experienced between interacting particles, through its impact on the second virial coefficient, B_2, as determined in the simulations (Supplementary Figure S5, *sec.2a*). Variations in experimentally determined B_2 with salt concentrations are available for NCPs in solution under various concentrations of salt (33). By mapping experimental B_2 with salt concentration and simulated B_2 with λ, allows us to derive λ versus salt concentration.

RESULTS AND DISCUSSION

SAXS measurements show that SV40 has higher chromatin density in the capsid center

Because SV40 is nearly spherical, as seen by the crystal structure (20), we fit the radially integrated X-ray scattering intensities as a function of the magnitude of the momentum transfer vector, q, (Figure 1) with a model of concentric spherical shells with a smoothly varying radial ED profile (Materials and Methods Equation 1). This approximation should yield a good fit at lower q values (corresponding to the larger elements of the icosahedral capsid), whereas at higher q values (~0.6 nm^{-1}, corresponding to ~10.5 nm in real space), where molecular details become important, the model is not expected to fit as well. Note, that SAXS measures the averaged structure of many virions, rather than the structure of a single specific virion.

As in earlier scattering studies (45–47), in addition to subtraction of the buffer intensity, we subtracted, from the buffer-subtracted data, a series of empirical power laws that pass through the minima of the scattering oscillating intensities and coincide with the highest available q-data ($q>3.5$ nm^{-1}), as previously described (42). This additional background originates in concentration fluctuations of our multi-component mixture (full particles, partially assembled particles, capsid proteins and nucleic acids) that lead to a q-dependent SAXS. Concentration fluctuations are Lorentzian-like (peaking close to $q=0$), hence contribute to power-law (q^{-2}) background. In addition, reactants (DNA and/or capsid proteins) and partially assembled structures may contribute to the background. The underlying assumption of our background subtraction is that most of the oscillating scattering signal comes from fully formed structures with uniform dimensions (i.e. the distribution of dimensions, e.g. particle radius, throughout the sample is very narrow). Our previous studies showed that both wt SV40 and DNA-VLPs are monodispersed [see transmission electron microscopy micrographs shown in Figure 6B and C in (40)]. We have therefore based the modeling on that premise. Moreover, had the sample been polydispersed, for example, by less than a nanometer in

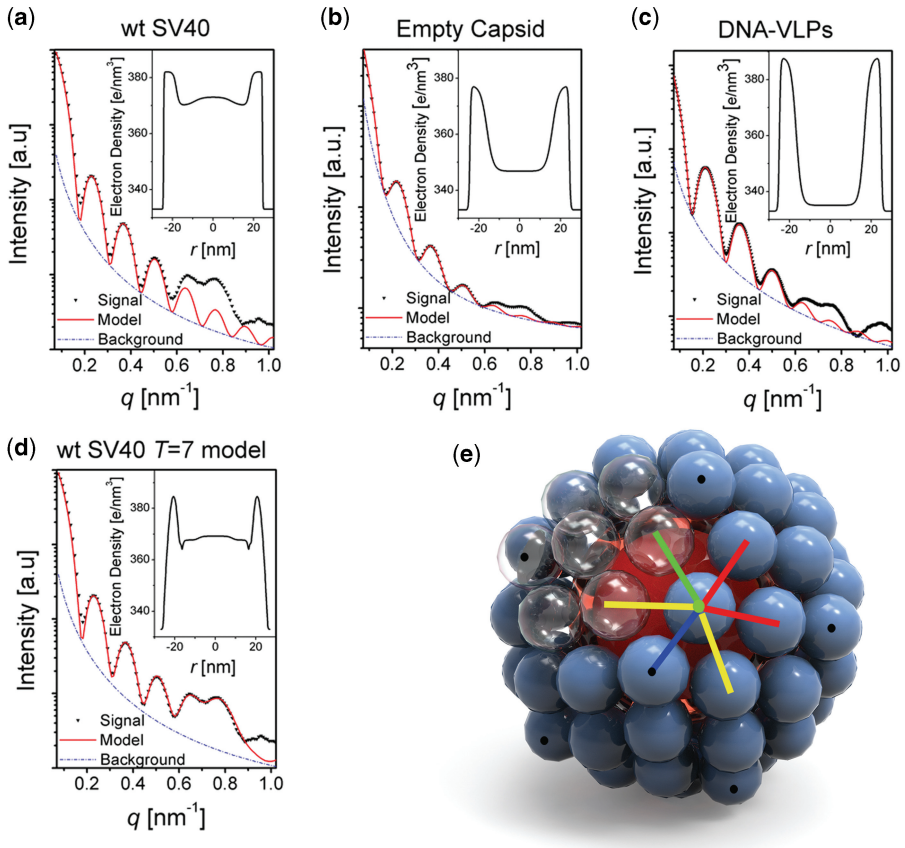

Figure 1. Radially integrated solution SAXS intensities (symbols) versus the magnitude of the momentum transfer vector q of (**a**) wt SV40, (**b**) empty capsid (**c**) VLPs containing dsDNA (DNA-VLPs) (**d**) wt SV40 $T = 7$ model. For (a–c), the solid red curves are the best fitted form-factor models of multiple spherical shells with a smoothly varying radial ED profiles, represented by hyperbolic tangent functions (Equation 1) and shown as insets to each plot. For (d), the solid red curve is the best fitted $T = 7$ form-factor model (Equation *2*). The average radial ED is shown as insets. The dashed blue curves show the assumed power-law background functions (see text and Tables 1 and 2). The best fitted parameters of the three models (a–c) are presented in Table 1 and for $T = 7$ form-factor model (d) in Table 2. The R^2 values for the models of wt SV40, empty capsid, DNA-VLPs and wt SV40 with the $T = 7$ model are 0.997, 0.979, 0.999, 0.996, respectively. (**e**) Representation of the fitted geometrical $T = 7$ model for wtSV40 (Equation 2). The red core represents the ED of the confined minichromosome, and the blue spheres represent the 72 VP1 pentamers building the virus capsid. The transparent spheres enable to view the capsid interior. Doted spheres mark the pentamer vertices of the icosahedron. The blue, yellow, red and green bars correspond to inter-pentamer distances of 9.0, 10.3, 9.7 and 8.5 nm, respectively, as the best fitted parameters establish. The SAXS data were measured at the ID02 beamline at the ESRF synchrotron (Grenoble). The experimental q range is $q = 0.07556$–$4.42314\,\mathrm{nm}^{-1}$.

the radius of the particle, the deep minima seen in Figure 1 would have been filled by a significant amount, as demonstrated in (43).

The best model fit for the wt SV40 virus (Equation 1) indicates high ED at the external spherical shell and in the center (Figure 1a). This finding suggests a high ED associated with the proteinaceous outer capsid layer (with typical ED values of $382 \pm 10\,\mathrm{e/nm}^3$, Table 1) and a uniform radial distribution of the nucleosomes within the capsid. In the model, the SV40 capsid's outer radius is 24.4 ± 0.1 nm, and the inner radius is 18.1 ± 0.1 nm compared with 24.7 nm and 17.9 nm determined for the crystal structure, respectively (20). These data allow a precise (sub nm) size estimate of the SV40, under physiological solution conditions. Furthermore, our results agree well with the density profiles determined in cryo-EM measurements of wt SV40 (48) (Figure 2a). Unlike the present study, the earlier crystal structure did not provide any information about the internal organization of the minichromosomes.

As expected, the spherical shell model fit does not account for features at higher q values, reflecting the icosahedral capsid deviations from a sphere. The discrepancy is seen beginning at $q > 0.65\,\mathrm{nm}^{-1}$ (Figure 1a). The deviation of the double maximum (at $q \approx 0.7\,\mathrm{nm}^{-1}$) arise from the arrangement of the capsid proteins, which, based on our more detailed $T = 7$ model (Equation 2 and Figure 1d), leads to the double hump observed in the SAXS data, corresponding to a mean distance between spheres of 9.5 nm (Figure 1e). This value is the typical distance between pentamer centers. In SV40, the pentamer cores, 6–7 nm in size, are separated by gaps due to their unique binding via long carboxy-terminal arms (20). The capsid's outer and inner radius, as measured by the detailed $T = 7$ model (Table 2), is similar to the radius calculated with the spherical shell model (Equation 1 Table 2 and Figure 1a). Moreover, the detailed $T = 7$ model and the spherical shell model both indicate a uniform distribution of the nucleosomes within the capsid with a possible

Table 2. The best fitted values for the scattering form factor of wtSV40, based on the $T = 7$ geometrical model (Equation 2 and Figure 1d)

Capsid parameters Parameters for the capsid spheres	Value	Inner core parameters: Parameters of the inner spherical shells	Value
[a]ED (e/nm^3)	391	[b]Layer 1- outer radius (nm)	8.3
[b]Radius (nm)	4.7	[b]Layer 2- outer radius (nm)	17.1
Slope (nm^{-1})	3.6	Slope layer1 (nm^{-1})	0.5
Icosahedron grid radius (nm)[c]	21.2	Slope layer2 (nm^{-1})	1.2
Inner radius of capsid (nm)[d]	16.5	[a]E.D. layer 1 (e/nm^3)	369
		[a]E.D. layer 2 (e/nm^3)	368
		Total radius of inner core (nm)	17.1
Background function		$0.0739 \times q^{-2.43} + 0.0343$	

The capsid parameters describe the size, position and ED of the spheres building the $T = 7$ icosahedral capsid (second term in Equation 2). The inner core parameters describe the averaged ED profile of the minichromosomal structure (the capsid interior given by the first term in Equation 2). An empirical power law background function was added to the form factor model (dashed blue carve in Figure 1d), as discussed in the text.
[a]The error in the ED is ± 2(e/nm^3).
[b]The error in the radii is ± 0.1 nm.
[c]The icosahedron radius is the distance between the center of the virus and the center of each sphere that is placed at each of the 12 vertices of the $T = 7$ structure.
[d]The inner radius is equal to the difference between the icosahedron grid radius and the radius of the spheres representing the VP1 pentamers.

slightly higher (statistical presence) nucleosome density in the center of the capsid.

Empty capsids, separated from wt SV40 by equilibrium sedimentation in a CsCl gradient (*SI sec.1 a*), generate scattering data that is best fit by low ED within the capsid (Figure 1b and Supplementary Figure S9a). The difference between the ED of the outer shell and the center is significantly larger for the empty capsids than for wt SV40. This result substantiates that the viral minichromosome accounts for the high ED at the center of the wt SV40 particles. Yet, the ED of the inner volume of the empty capsid is higher than the solvent ED, possibly because of unidentified molecules of the host cell trapped within the empty capsids. These can also account for the thicker wall of the empty capsid (8.4 nm) compared with the wall thickness of the wt SV40 (6.3–6.6 nm, for the $T = 7$ model the wall width is calculated at half maximum).

In the absence of nucleosomes, dsDNA packs close to the capsid shell

Synthetic VLPs containing dsDNA (DNA-VLPs) are assembled *in vitro* from recombinant SV40 capsid VP1 proteins (produced in insect cells) and closed-circular (histone-less) dsDNA (40) (*SI sec.1b*). These DNA-VLPs do not contain VP2 and VP3, which are present in both wt SV40 and empty particles purified from CV1 primate cells. The scattering curve of these DNA-VLPs shows that their wall ED is higher than that of wt SV40, whereas its thickness resembles that of the empty capsid. Their ED at the center is lower than that of both empty capsids and wt SV40 (Figure 1c and Supplementary Figure S9b). We interpret this finding as follows: owing to large persistence length of dsDNA (~50 nm), nucleosome-free DNA within the DNA-VLPs is forced against the outer wall, thus adding to its thickness (compared with the wt virus) and leaving the center clear. This explanation is supported by our earlier findings indicating that during assembly *in vitro* of DNA-VLPs, the plasmid DNA must undergo compaction (40). This DNA organization is reminiscent of that found in dsDNA bacteriophages, where the DNA concentrates close to the viral capsid owing to its large persistence length (1,49). In contrast, in wt SV40, the nucleosomes condense the DNA, relieving the force that drives DNA to the capsid wall and allowing it to spread across the interior of the virion. These results indicate that the higher-order nucleoprotein structure of the minichromosome dictates nucleosome distribution in the capsid.

Coarse-grained simulations describe viral chromatin packaging

To investigate the possible structure of the minichromosome within the SV40 capsid, we modeled the confined chromatin arrangement using a coarse grained model, and validated the model by comparing with our SAXS experiments. Different levels of coarse graining have previously been used to model various aspects of oligonucleosomal arrangement (24,29,50–59). These simulations were used to investigate the role of histone tails, salt concentration, nucleosome repeat length, entry-exit angle of DNA at the histone surface and more. Specifically, simulations indicate that the longer the DNA linker between nucleosomes, the larger the diameter of the resulting chromosome fiber (56,57). Moreover, experiments (27) have shown that for the calculated average linker length of the SV40 minichromosome, ~90 bp (see *SI sec.1e*), the expected fiber diameter is ~45 nm, raising the question of how the minichromosome can fit into a ~36 nm diameter capsid. Additional simulations indicate that at higher salt concentration (200 mM), the attractive electrostatic interactions between the nucleosomes are more dominant, thus leading to more condensed structures (58). None of these models, however, investigated the chromatin arrangement within confined cavities, similar to the conditions existing within the SV40 virion.

Here, we use a simple mesoscopic model, wherein viral chromatin is composed of oblate ellipsoids, each representing a nucleosome. Based on experimental data (35), the ellipsoids have a ratio of short to long radius of

$\sigma_f/\sigma_e = 0.5$, and interact through Gay–Berne-type potentials (60,61). This orientationally dependent interaction potential accounts for excluded volume repulsions and longer ranged attractive forces between nucleosomes; these forces were parameterized based on experimentally determined interactions between NCPs in solution (33,34) (*SI sec.1d*). In our model, ellipsoids (histone octamers) are tethered via harmonic potentials, representing linker DNA stretches between nucleosomes. In the model, we define the average distance between the nucleosomes, $r_0 = 30$ nm (or 3σ with $\sigma \equiv \sigma_e = 10$ nm) where 30 nm corresponds to ~90 bp (*SI sec.1e)*, and their average sliding distance along the DNA as ± 15 nm (*SI sec.1e*).

The SV40 icosahedral capsid is modeled as a spherical-bounding shell interacting with nucleosomes via short range (steric) repulsive forces and long range, mostly electrostatic, attractive forces, acting normal to the shell surface (*SI sec.1f*). Guided by parameters derived from our SAXS experiments (Table 1), we set the effective internal radius of the capsid sphere (the maximum allowed radius for the minichromosome) at 20 nm. Based on previous reports, we assumed $N = 20$ ellipsoids in a capsid (16–18).

Molecular configurations are generated using the standard Metropolis algorithm (44). Thus, our simulations predict the average nucleosomal distribution of an ensemble of many virions at their free energy minima, but cannot determine the chromatin order of a specific virion or the kinetics of nucleosome movement within an individual capsid. The effect of salt concentration in the bulk is represented through the parameter λ ('Materials and Methods' section). Values of $\lambda = 1.5$–1.75 correspond to 100–150-mM bulk salt concentration (the physiological and our experimental ionic strength), as calibrated from NCP solution data, and considering the reported error in those measurements (33) (see also *SI sec 2a*). Higher or lower λ values correspond to lower and higher salt concentrations, respectively. Even though we associate λ with salt concentration, it can similarly be correlated through similar mappings with other thermodynamic variables such as temperature, pH or osmotic stress. We assume room temperature in all simulations, as in our experiments.

To gain insight into the forces and constraints that determine the nucleosomal order observed in simulations, our strategy was to consider several reduced models. In each of these models, a subset of interactions was either modified or completely turned off, allowing us to evaluate its impact on nucleosomal arrangement by comparison with the 'full model' (FM) described in the earlier 3 paragraphs, which considered all interactions. Thus, to follow the impact of nucleosome connectivity, we used a reduced model that modifies the DNA-tethering forces between nucleosomes (tethering model, TM), and a model that assumes that the nucleosomes are free to slide along the DNA (no-tethering, NT). Similarly, to estimate the interactions of nucleosomes with the boundary, we studied a model that, in addition to free sliding, included a purely repulsive force with the capsid walls (NT and no-attractive-boundary, NT-NAB).

Experiments and simulations show similar chromatin densities in the virion

In excellent agreement with the SAXS experiments, the FM indicates high average nucleosome densities in the center of the capsid that decreases towards the periphery (compare FM and SAXS, Figure 2a). In comparing simulations with experimental ED profiles, we present the simulated average local ED distribution along the radius of the capsid $d(r)$, normalized such that $\int_o^{Rcap} d(r) 4\pi r^2 dr = 1$. The remarkable agreement between experiments and simulations suggests that the packaging constraints of the nucleosomes, together with simple interactions considered in the simulations, are the main driving forces leading to the structure and order of chromatin in the SV40 virus. At salt concentrations of 50–300 mM, corresponding to $\lambda > 1.5$, the change in radial density is minimal (Supplementary Figure S8, $\lambda = 1.5$, 1.75 and 3). In contrast, at lower λ (corresponding to salt concentration >>300 mM), the nucleosomes become more ordered and start assuming a solid-like organization (Supplementary Figure S8, $\lambda = 0.7$ and 0.3). We conclude that modest deviations from physiological conditions are predicted to be insufficient to change the organization of the packaged minichromosome.

Rigid nucleosome tethering would lead to strong nucleosome stacking at the capsid wall and less accumulation in the capsid center

Modifying tethering interactions let us estimate the extent of packing frustration that nucleosomal connectivity ensues. We compared three variations of tethering interactions for nucleosomal connectivity (Figure 2b). In the first tethering model (TM-1 nm), nucleosomes are tethered by rigid harmonic linkers with an equilibrium distance of 30 nm and a potential well-width corresponding to mean fluctuations (sliding distance) of ± 1 nm at thermal energy, k_BT. This model corresponds to rigid DNA linkers with the known DNA persistence length (~50 nm at physiological conditions) and with no nucleosome sliding allowed. In the second model, the nucleosomes are tethered strongly, with mean nucleosome–nucleosome distances set at 30 nm and mean fluctuations of ± 10 nm (TM-10 nm). This corresponds to the minimum sliding indicated experimentally for the few SV40 nucleosomes experimentally found to be strongly localized (62), (see *SI sec.1e* for further details). In the third model, nucleosomes are freer to move (slide) with respect to one another, with the average distances (30 nm) but fluctuations of ± 35 nm (TM-35 nm). For comparison, we also present results for untethered nucleosomes (NT).

In contrast to the experiments (Figure 2a, SAXS), simulations of the strongly tethered nucleosomes (Figure 2b, TM-1 nm and TM-10 nm) show particles tightly packed against the capsid internal wall in a dense (hypertrophic) layer. This finding suggests that this model incorrectly captures nucleosomal mobility, in agreement with previous experimental determination of nucleosome phasing in the virus (62). Those experiments showed that strongly localized nucleosomes are widely separated from one another, with long stretches of loosely localized ones.

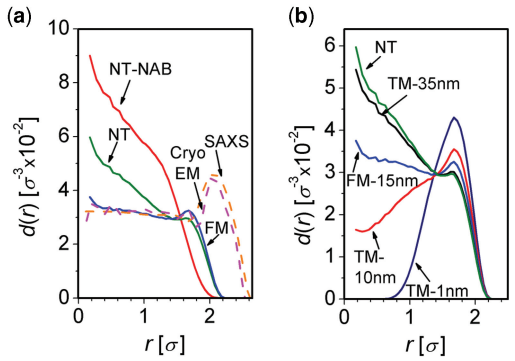

Figure 2. Chromatin local density $d(r)$ in simulations as would be observed along the radius of the capsid. (**a**) For three models at $\lambda = 1.75$: Blue curve, FM; Green, in the absence of tethering (NT); Red in the absence of tethering and lacking attractive forces to the boundary (NT-NAB). Also shown are the best model fit for the SAXS data for SV40 (taken from the inset to Figure 1d), normalized to the FM density at low r (orange dashed line); the spherically averaged density profile of SV40 measured by Cryo-EM adapted from Shen *et al.* (48) and normalized to FM density at low r (magenta dashed line). (**b**) $d(r)$ at $\lambda = 1.75$ for green, NT model; Black, strong tethering well (minimal sliding, TM-1 nm); Red, weaker tethering (less sliding, TM-10 nm); Navy, weak tethering (maximal sliding, TM-35 nm); Blue, the FM. See text for additional details.

Indeed, SAXS experiments fit much better with simulations of more loosely tethered nucleosomes that assume nucleosome sliding of ± 15 nm (compare FM and TM-10 Figure 2b with SAXS, Figure 2a). In contrast, when tethering is weak or absent (Figure 2b, TM-35 nm or NT, respectively) we find a higher nucleosome density in the center of the capsid and a reduced density near the capsid walls with respect to our experimental data. Even though the structure of the minichromosome (closed circle) is probably more constrained than linear chromatin, simulation results for circular and linear chromatin, as expected, are identical (within statistical error). To fully appreciate the possible importance of the topology of circular chromatin, additional forces absent from our model, such as supercoiling and the resulting torsion (63), should be considered. However, our current stage of understanding of chromatin structure does not allow to reliably incorporate the topology. Nevertheless, the FM well reproduces the available experimental results, from both SAXS and cryo-EM, supporting its use as a minimal model for the SV40 minichromosome. Moreover, previous modeling studies suggest that the overall higher-order structure of chromatin is dominated by inter-nucleosome interactions, and is rather insensitive to details of the linker free energy (64).

Attractive capsid walls increase nucleosome density at the hypertrophic layer, while maintaining the higher density in the capsid center

The capsid protein VP1 possesses a DNA-binding domain (65). Moreover, the calculated electrostatic potential on the capsid interior shows 'salt-and-pepper' speckles of positively and negatively charged residues (Supplementary Figure S3), which could lead to attractive forces with the minichromosome. Supplementary Figure S3 shows an internal view of the capsid crystallographic structure (left) and the corresponding electrostatic potential as calculated using Poisson–Boltzmann theory (right) (66). To evaluate the role of these attractive forces between the capsid and the minichromosome, we simulated untethered nucleosomes that lack an attractive force with the boundary (NT-NAB), as described in *SI sec.1f*. These conditions result in high nucleosomal density in the capsid center, even higher than those found when an attractive boundary is used, (compare NT-NAB with NT Figure 2a). The lack of attractive forces with the boundary also results in lower local density in the hypertrophic layer than when attractions are included (Figure 2a). Clearly, even in the presence of moderate attractive forces with the wall, the density maximum at the center of the capsid persists, reflecting dominance of the inter-nucleosomal attraction and spatial confinement (Figure 2a, NT).

An additional reduction of the FM substitutes Gay–Berne potentials (ellipsoids) with nucleosomes modeled as spheres, interacting through Lennard–Jones potentials, and trapped within a spherical repelling boundary (*SI sec.2b*). As in the FM, this reduced model indicates strong particle density in the center of the cavity (Lennard-Jones Model-LJM in Supplementary Figure S6). The fact that both ellipsoids and spheres lead to elevated local density in the cavity center supports our conclusion that this particle arrangement, found in SV40, reflects dominance of the confining shell wall. Notably, this confinement effect is abolished when the system is confined in only one dimension, such as a simple liquid between two walls, where density in the center is never the global maximum.

Contrary to nucleosomes in bulk solution, nucleosomes within SV40 are disordered

The good correspondence of simulations with the experiments (Figure 2a, FM and SAXS) provides validation to the simulations, indicating that the major forces responsible for particle ordering in the virion are appropriately accounted for. With this, we turn to explore additional information that is hardly accessible by available experimental techniques. Specifically, we use the model to predict possible nucleosomal orientations within the capsid. The reference point for our analysis is the well-studied state of nucleosomes in the bulk.

To make links to bulk experimental measurements of NCPs in solution (38), we simulate untethered ellipsoids under periodic boundary conditions (PBC) representing the bulk. To follow the possible ordering of particles, we use the orientational order parameter,

$$S = \left\langle \frac{3\cos^2\theta - 1}{2} \right\rangle \quad (4)$$

where θ is the angle between the ellipsoid director and the director defining the average orientation of all particles, $\hat{z}$ (as detailed in *SI sec.2c*). Although the simulated systems considered here are finite ($N = 100$), we borrow terminology from the descriptions of orientational phases and their transitions in infinite systems, as follows. At high λ (low salt concentration), where interactions between particles is weak, the ellipsoids are in an isotropic-like regime

and do not show preferred alignment (low S). Yet, as λ decreases and attractive interparticle interactions become dominant, we find an orientational transition, and the ellipsoids preferentially align along a common axis, corresponding to a bulk nematic phase (nematic-like regime). Concomitantly, S increases and particles enjoy stronger favorable contacts (asterisks mark transitions points in Figure 3a, PBC). Similarly, as λ is further lowered (corresponding to very high salt concentration), the system becomes increasingly more ordered and undergoes an additional transition into a columnar-like regime and finally to a solid-like regime (compare snapshots in Figure 3b). These results are consistent with simulation results of oblate ellipsoids in the bulk (67).

Reported studies of unconfined NCPs in aqueous solutions (38) indicate that nucleosomes order in a columnar phase at densities and ionic strengths similar to those of the native virus (~150 mM salt and ~200 mg/ml NCPs corresponding to $\lambda = 1.5$–1.75 and nucleosome reduced density $\rho_{Nuc} \approx 0.6$, respectively; for definition of ρ_{Nuc}, see *SI sec.2a*). As expected, S values indicate that for our bulk simulations at $\lambda = 1.5$–1.75 untethered ellipsoids are ordered in the nematic-like regime, or situated close to the isotropic-nematic transition (Figure 3a, PBC $N = 100$, shaded area). In contrast, for $N = 20$ nucleosomes within a spherical shell (representing SV40) at the same λ's, the nucleosomes assume a 'molten droplet' state, whereby particles are on average orientationally disordered (FM, NT-NAB, NT Figure 3a shaded area). This effect is found regardless of DNA tethering or boundary attraction, indicating that confinement is sufficient for reducing the order of chromatin.

The small number of nucleosomes is sufficient to change the salt concentration threshold for the phase transition

We find that the order–disorder transition (isotropic-like to nematic-like) occurs at a specific 'critical' value λ_c. Following several numbers of particles at similar densities indicates that, the lower the number of particles, the lower the determined λ_c (Figure 3a and Supplementary Figure S7). This is analogous to the known finite-size effect, which manifests as a shift in the critical phase transition temperature of other known order–disorder transitions (68–70). Here, these shifts are the result of the limited system size that restricts the correlation length for orientational fluctuations, which must necessarily diverge to allow a second-order transition (71). We conclude that, in accordance with this finite-size effect, the smaller number of nucleosomes is sufficient to decrease (compared with bulk solutions) the value of λ_c required for the order–disorder transition. This finding suggests that at physiological ionic strength, the confined nucleosomes are in a disordered state, whereas NCPs in the bulk ($N >> 100$) are ordered; for example, for $N = 300$ we find $\lambda_c \approx 1.9$.

Capsid confinement can further decrease nucleosomal ordering

Although for the bulk, there are two clear orientational transitions (market by asterisk, Figure 3a, PBC), for the confined, untethered ellipsoids, we find only one clear transition from isotropic-like to nematic-like organization. As λ is further lowered (corresponding to higher salt), the particles under confinement become increasingly more ordered, moving to a columnar-like arrangement regime (Figure 3a, snapshots), but not to the solid-like regime (Figure 3b, left). Moreover, while for the ellipsoids simulated in the bulk at low λ, we find that S approaches 1 (Figure 3a, PBC) for the ellipsoids confined within a spherical shell, the highest order parameter reached, regardless of DNA tethering or boundary attraction, is $S = 0.8$ (Figure 3a FM, NT and NT-NAB). This effect is also found for all simulations of ellipsoids confined within a spherical boundary, at various numbers of particles, densities and cavity diameter (Supplementary Figure S7). Thus, we conclude that the confining spherical boundary is sufficient to induce disorder in the system and hinder the solid-like regime.

Nucleosomes in the hypertrophic layer align with the capsid walls

To resolve the boundary effects on nucleosomal order, we define the radial order parameter, Σ, in terms of the ellipsoid alignment with the spherical shell's radius vector (*SI sec.2d*). From the variation of Σ with distance from the boundary, we find that, for both low and high λ, the ellipsoids within the 'wetting layer' near the boundary show an average radial order parameter close to $\Sigma = 1$ (Figure 4, red and black curves). This finding suggests that particles mostly lie flat against the boundary, thus reducing their excluded volume interactions with the bounding wall. However, only at low λ, the order parameter S for ellipsoids outside the wetting layer (defined as $r < 1.5\sigma$) indicates that particles preferentially align with respect to one another significantly (compare red and black horizontal line, Figure 4). Thus, particle ordering is affected by the balance between inter-particle interactions favoring high S and wall-particle interactions favoring high Σ, as demonstrated in snapshot of Supplementary Figure S7b. These competing forces become more prominent at low λ, where both S and Σ are higher. As a result, the system can exist in the ordered columnar-like regime ($S = 0.8$) arrangements, but owing to the requirement to also order with the boundary, cannot reach the high degree of order seen in the solid-like regime arrangements ($S = 1$).

The balance of wall and bulk interactions determine nucleosomal order and the critical point

Simulations show that λ_c decreases when interactions with the boundary become more dominant, specifically, by increasing the nucleosome local density in the hypertrophic layer as a results of an attractive potential at the boundary, or of DNA tethering, (compare FM, NT with NT-NAB, Figure 3a). This decrease in λ_c indicates that orientational frustration with the wall becomes stronger in comparison with inter-particle attractions, even at lower λ. Therefore, the model predicts that a higher ionic strength (corresponding to screening of repulsive interactions) is required before the confined ellipsoids can overcome the aligning tendencies with the boundary,

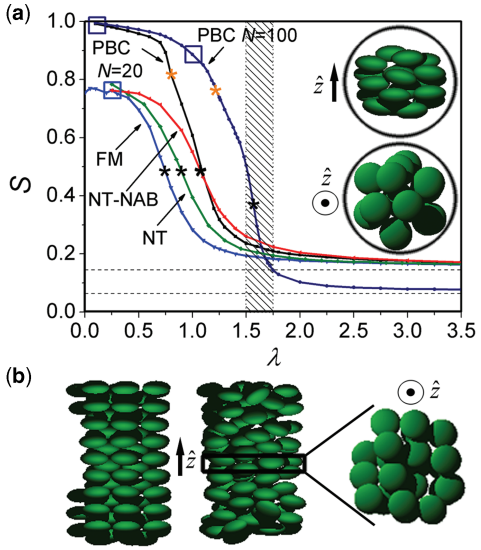

Figure 3. Nucleosomal order in simulations. (**a**) Order parameter S versus λ (associated with the concentration of salt) at a constant density of $\rho_{Nuc} \approx 0.6$. Navy is for PBC $N = 100$; Black, PBC $N = 20$; Red, NT-NAB model; Green, NT model; Blue, FM. Top right insets show snapshots of the system from two different perspectives for the FM at $\lambda = 0.25$, taken from simulations conditions marked in plots by blue square. The highlighted area marks the range $1.5 < \lambda < 1.75$, corresponding to the range of physiological salt concentrations. Dashed lines mark the average S for 100 or 20 randomly oriented ellipsoids. Black and orange asterisks mark the critical point for two consecutive transitions (isotropic-like to nematic-like and nematic-like to columnar-like, respectively), calculated via the derivative of S. (**b**) Snapshots of 100 ellipsoids under bulk-like conditions (i.e. under PBC) at constant density, $\rho_{Nuc} \approx 0.6$. Left, snapshot of the system for $\lambda = 0.1$, taken from simulations conditions marked in plots by navy square. Right, snapshot of the system for $\lambda = 1$ with additional snapshot of a slice through the center in the xy plane. All snapshots are oriented so that the eigenvector of the highest order parameter is defined as $\hat{z}$.

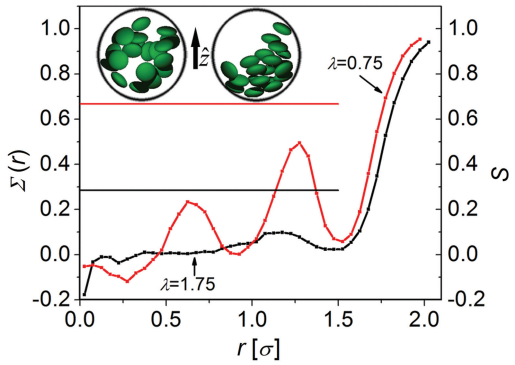

Figure 4. Nucleosome orientational order along the capsid radius from simulations. Full dotted lines follow the radial order parameter $\Sigma(r)$ versus distance from the boundary, for the FM. Short straight lines indicate the average order parameter (S) for all the ellipsoids that are located away from the boundary ($r < 1.5\sigma$), shown for $\lambda = 1.75$ (black) and $\lambda = 0.75$ (red). Inset shows snapshots for the FM at $\lambda = 1.75$ (left) and $\lambda = 0.75$ (right). Snapshots are oriented with the eigenvector of the highest order parameter defined as $\hat{z}$.

allowing particles to order in a nematic-like regime (preferred by particle–particle attractive and steric packing interactions). This change in the critical value of λ owing to confinement is analogous to the Gibbs–Thomson effect that describes the lowering of the liquid-solid phase transition temperature owing to surface tension (72).

In conclusion, particle–particle order is lowered because of frustration between wall and nucleosomal shape (bulk columnar tendencies that are incommensurate with spherical boundary alignment). This leads on average to more isotropic nucleosomal packaging within the spherical shell, in contrast to the nematic, columnar or higher-ordered arrangements that are expected for the same density and interactions in bulk solutions in the absence of confining boundaries (38). Interestingly, similar frustration between bulk and confining walls was also shown to determine the order of other highly confined nematogens, including nematic droplettes, or tactoids (7,73,74).

CONCLUDING REMARKS

Showing remarkable agreement, both SAXS experiments and coarse-grained simulations of SV40 chromatin point to high nucleosome density at the center of the capsid. Simulations further indicate a weak hypertrophic layer close to the capsid internal wall. In contrast, the organization of the nucleosome-free dsDNA in DNA-VLPs shows low nucleic acid density at the capsid center, and high DNA concentration close to the viral capsid (Figure 1c). These results indicate that addition of nucleosomes to dsDNA leads to chromatin condensation and allows the DNA to extend to the center of the capsid, whereas the attractive boundary and tethering between nucleosomes favor a hypertrophic layer at the capsid wall. Moreover, computer modeling suggests that accounting for nucleosomal packaging under confinement is sufficient to explain the minichromosome organization seen by SAXS.

Although experiments of unconfined NCPs (38), as well as our simulations, indicate that nucleosomes in the bulk at the densities found inside the virus are orientationally ordered, the simulations of confined ellipsoids predict lack of particle-to-particle alignment (Figure 4 left snapshot). Yet, within the wetting layer, ellipsoids align with the boundary (Figure 4 right), reflecting their preferential interaction with the wall. Overall, the presence of a nanometric confining boundary stabilizes the isotropic-like state with respect to the nematic-like regime. This disordering tendency is caused by the incommensurate wall versus bulk symmetry, as well as by the small number of particles that restricts the maximum possible correlation length (75). As a result, we predict that the minichromosome within the SV40 capsid exists above the order–disorder transition (λ is higher than λ_c), which we term a 'molten droplet' state. A similar balance between opposing forces is found in confined nematogens such as in tactoids, where bulk nematic tendencies compete with surface alignment 'anchoring' forces (7,73,74).

Beyond understanding the structural characteristics of the packaged SV40 minichromosome, this combined study underscores the important effect that strong confinement may have on the adaptable and malleable character of chromatin ordering. Together with numerous important

modifiers of chromatin order that have previously been studied (30), it remains to be determined whether such 'crowding' affects chromatin structure *in vivo* (76). Indeed, it will be interesting to find evidence for such nematic 'melting' for other viruses, or for polymers and liquid crystals that are subject to nanoconfinement.

SUPPLEMENTARY DATA

Supplementary Data are available at NAR Online: Supplementary Figures 1–9, Supplementary Methods, Supplementary Results and Supplementary References [77–90].

ACKNOWLEDGEMENTS

The authors thank the SOLEIL synchrotron, SWING beam-line and J. Perez; ESRF, beam-line ID02 and J. Gummel, S. Callow and T. Naryanan; and Elettra, 5.2L SAXS beam-line, and H. Amenitsch, for discussions and help with SAXS data acquisition. R.A. thanks the Hebrew University Nanocenter for a fellowship support. The Fritz Haber Center is supported by the Minerva foundation, Munich, Germany. G.S., S.K., A.O., U.R. and D.H. designed research; G.S., S.K., U.R. and D.H. preformed research; G.S. and R.A. analyzed data; G.S., A.O., U.R. and D.H wrote the article.

FUNDING

US–Israel Binational Science Foundation [2005050 to A.O.]; the James Franck Minerva program (to D.H. and U.R.). Funding for open access charge: James Franck Minerva program.

Conflict of interest statement. None declared.

REFERENCES

1. Kindt,J., Tzlil,S., Ben-Shaul,A. and Gelbart,W.M. (2001) DNA packaging and ejection forces in bacteriophage. *Proc. Natl Acad. Sci. USA*, **98**, 13671–13674.
2. Cerritelli,M.E., Cheng,N.Q., Rosenberg,A.H., McPherson,C.E., Booy,F.P. and Steven,A.C. (1997) Encapsidated conformation of bacteriophage T7 DNA. *Cell*, **91**, 271–280.
3. Smith,D.E., Tans,S.J., Smith,S.B., Grimes,S., Anderson,D.L. and Bustamante,C. (2001) The bacteriophage phi 29 portal motor can package DNA against a large internal force. *Nature*, **413**, 748–752.
4. Jiang,W., Chang,J., Jakana,J., Weigele,P., King,J. and Chiu,W. (2006) Structure of epsilon15 bacteriophage reveals genome organization and DNA packaging/injection apparatus. *Nature*, **439**, 612–616.
5. Petrov,A.S. and Harvey,S.C. (2007) Structural and thermodynamic principles of viral packaging. *Structure*, **15**, 21–27.
6. Petrov,A.S., Lim-Hing,K. and Harvey,S.C. (2007) Packaging of DNA by bacteriophage epsilon15: structure, forces, and thermodynamics. *Structure*, **15**, 807–812.
7. Svensek,D., Veble,G. and Podgornik,R. (2010) Confined nematic polymers: order and packing in a nematic drop. *Phys. Rev. E*, **82**, 011708.
8. Knobler,C.M. and Gelbart,W.M. (2010) In: Stockley,P.G. and Twarock,R. (eds), *Emerging Topics in Physical Virology*. Imperial College Press, London, pp. 208–215.
9. Dykeman,E.C., Grayson,N.E., Toropova,K., Ranson,N.A., Stockley,P.G. and Twarock,R. (2011) Simple rules for efficient assembly predict the layout of a packaged viral RNA. *J. Mol. Biol.*, **408**, 399–407.
10. Bunka,D.H.J., Lane,S.W., Lane,C.L., Dykeman,E.C., Ford,R.J., Barker,A.M., Twarock,R., Phillips,S.E.V. and Stockley,P.G. (2011) Degenerate RNA packaging signals in the genome of satellite tobacco necrosis virus: implications for the assembly of a T = 1 capsid. *J. Mol. Biol.*, **413**, 51–65.
11. Zlotnick,A., Cheng,N., Stahl,S.J., Conway,J.F., Steven,A.C. and Wingfield,P.T. (1997) Localization of the C terminus of the assembly domain of hepatitis B virus capsid protein: implications for morphogenesis and organization of encapsidated RNA. *Proc. Natl Acad. Sci. USA*, **94**, 9556–9561.
12. Tihova,M., Dryden,K.A., Le,T.V.L., Harvey,S.C., Johnson,J.E., Yeager,M. and Schneemann,A. (2004) Nodavirus coat protein imposes dodecahedral RNA structure independent of nucleotide sequence and length. *J. Virol.*, **78**, 2897–2905.
13. Belyi,V.A. and Muthukumar,M. (2006) Electrostatic origin of the genome packing in viruses. *Proc. Natl Acad. Sci. USA.*, **103**, 17174–17178.
14. Siber,A. and Podgornik,R. (2008) Nonspecific interactions in spontaneous assembly of empty versus functional single-stranded RNA viruses. *Phys. Rev. E*, **78**, 051915.
15. Griffin,B. (1981) In: Tooze,J. (ed.), *DNA Tumor Viruses*, 2nd edn. Cold Spring Harbor Laboratory, Cold Spring Harbor, NY, pp. 61–123.
16. Cremisi,C., Pignatti,P.F., Croissant,O. and Yaniv,M. (1976) Chromatin-like structures in polyoma-virus and simian virus 40 lytic cycle. *J. Virol.*, **17**, 204–211.
17. Griffith,J.D. (1975) Chromatin structure—deduced from a minichromosome. *Science*, **187**, 1202–1203.
18. Christiansen,G., Landers,T., Griffith,J. and Berg,P. (1977) Characterization of components released by alkali disruption of simian virus-40. *J. Virol.*, **21**, 1079–1084.
19. Liddington,R.C., Yan,Y., Moulai,J., Sahli,R., Benjamin,T.L. and Harrison,S.C. (1991) Structure of simian virus-40 at 3.8-a resolution. *Nature*, **354**, 278–284.
20. Stehle,T., Gamblin,S.J., Yan,Y.W. and Harrison,S.C. (1996) The structure of simian virus 40 refined at 3.1 angstrom resolution. *Structure*, **4**, 165–182.
21. Bina,M. (1986) Simian virus 40 assembly. *Comments Mol. Cell Biophys.*, **4**, 55–62.
22. Hansen,J. (2012) Human mitotic chromosome structure: what happened to the 30-nm fibre? *EMBO J.*, **31**, 1621–1623.
23. Maeshima,K., Hihara,S. and Eltsov,M. (2010) Chromatin structure: does the 30-nm fibre exist in vivo? *Curr. Opin. Cell Biol.*, **22**, 1–7.
24. Schiessel,H., Gelbart,W.M. and Bruinsma,R. (2001) DNA folding: structural and mechanical properties of the two-angle model for chromatin. *Biophys. J.*, **80**, 1940–1956.
25. Kruithof,M., Chien,F.T., Routh,A., Logie,C., Rhodes,D. and van Noort,J. (2009) Single-molecule force spectroscopy reveals a highly compliant helical folding for the 30-nm chromatin fiber. *Nat. Struct. Mol. Biol.*, **16**, 534–540.
26. Felsenfeld,G. and McGhee,J.D. (1986) Structure of the 30 nm chromatin fiber. *Cell*, **44**, 375–377.
27. Robinson,P.J.J., Fairall,L., Huynh,V.A.T. and Rhodes,D. (2006) EM measurements define the dimensions of the "30-nm" chromatin fiber: evidence for a compact, interdigitated structure. *Proc. Natl Acad. Sci. USA*, **103**, 6506–6511.
28. Wedemann,G. and Langowski,J. (2002) Computer simulation of the 30-nanometer chromatin fiber. *Biophys. J.*, **82**, 2847–2859.
29. Schlick,T. and Perisic,O. (2009) Mesoscale simulations of two nucleosome-repeat length oligonucleosomes. *Phys. Chem. Chem. Phys.*, **11**, 10729–10737.
30. Schlick,T., Hayes,J. and Grigoryev,S. (2012) Toward convergence of experimental studies and theoretical modeling of the chromatin fiber. *J. Biol. Chem.*, **287**, 5183–5191.
31. Martin,R.G. (1977) Nucleoprotein core of simian virus-40. *Virology*, **83**, 433–437.
32. Dubochet,J., Adrian,M., Schultz,P. and Oudet,P. (1986) Cryoelectron microscopy of vitrified Sv40 minichromosomes - the liquid-drop model. *EMBO J.*, **5**, 519–528.

33. Bertin,A., Leforestier,A., Durand,D. and Livolant,F. (2004) Role of histone tails in the conformation and interactions of nucleosome core particles. *Biochemistry*, **43**, 4773–4780.
34. Bertin,A., Mangenot,S., Renouard,M., Durand,D. and Livolant,F. (2007) Structure and phase diagram of nucleosome core particles aggregated by multivalent cations. *Biophys. J.*, **93**, 3652–3663.
35. Luger,K., Mader,A.W., Richmond,R.K., Sargent,D.F. and Richmond,T.J. (1997) Crystal structure of the nucleosome core particle at 2.8 angstrom resolution. *Nature*, **389**, 251–260.
36. Mangenot,S., Leforestier,A., Durand,D. and Livolant,F. (2003) Phase diagram of nucleosome core particles. *J. Mol. Biol.*, **333**, 907–916.
37. de Gennes,P.G. and Prost,J. (1993) *The Physics of Liquid Crystals*, 2nd edn. Oxford Science Publications, New York, NY, pp. 41–97.
38. Leforestier,A. and Livolant,F. (1997) Liquid crystalline ordering of nucleosome core particles under macromolecular crowding conditions: evidence for a discotic columnar hexagonal phase. *Biophys. J.*, **73**, 1771–1776.
39. Ben-nun-Shaul,O., Bronfeld,H., Reshef,D., Schueler-Furman,O. and Oppenheim,A. (2009) The SV40 Capsid Is Stabilized by a Conserved Pentapeptide Hinge of the Major Capsid Protein VP1. *J. Mol. Biol.*, **386**, 1382–1391.
40. Mukherjee,S., Abd-El-Latif,M., Bronstein,M., Ben-nun-Shaul,O., Kler,S. and Oppenheim,A. (2007) High cooperativity of the SV40 major capsid protein VP1 in virus assembly. *PLoS One*, **2**, e765.
41. Mukherjee,S., Kler,S., Oppenheim,A. and Zlotnick,A. (2010) Uncatalyzed assembly of spherical particles from SV40 VP1 pentamers and linear dsDNA incorporates both low and high cooperativity elements. *Virology*, **397**, 199–204.
42. Ben-Nun,T., Ginsburg,A., Szekely,P. and Raviv,U. (2010) X plus : a comprehensive computationally accelerated structure analysis tool for solution X-ray scattering from supramolecular self-assemblies. *J. Appl. Crystallogr.*, **43**, 1522–1531.
43. Szekely,P., Ginsburg,A., Ben-Nun,T. and Raviv,U. (2010) Solution X-ray scattering form factors of supramolecular self-assembled structures. *Langmuir*, **26**, 13110–13129.
44. Metropolis,N., Rosenbluth,A.W., Rosenbluth,M.N., Teller,A.H. and Teller,E. (1953) Equation of state calculations by fast computing machines. *J. Chem. Phys.*, **21**, 1087–1092.
45. Fernando-Diaz,J., Andreu,J.M., Diakun,G., Towns-Andrews,E. and Bordas,J. (1996) Structural intermediates in the assembly of taxoid-induced microtubules and GDP-tubulin double rings: time-resolved X-ray scattering. *Biophys. J.*, **70**, 2408–2420.
46. Andreu,J.M., Bordas,J., Diaz,J.F., Garcia de Ancos,J., Gil,R., Medrano,F.J., Nogales,E., Pantos,E. and Towns-Andrews,E. (1992) Low resolution structure of microtubules in solution: synchrotron X-ray scattering and electron microscopy of taxol-induced microtubule assembled from purified tubulin in comparison with glycerol and MAP-induced microtubules. *J. Mol. Biol.*, **226**, 169–184.
47. Raviv,U., Needleman,D.J., Li,Y., Miller,H.P., Wilson,L. and Safinya,C.R. (2005) Cationic liposome - microtubule complexes: pathways to the formation of two state lipid-protein nanotubes with open or closed ends. *Proc. Natl Acad. Sci. USA*, **102**, 11167–11172.
48. Shen,P.S., Enderlein,D., Nelson,C.D.S., Carter,W.S., Kawano,M., Xing,L., Swenson,R.D., Olson,N.H., Baker,T.S., Cheng,R.H. *et al.* (2011) The structure of avian polyomavirus reveals variably sized capsids, non-conserved inter-capsomere interactions, and a possible location of the minor capsid protein VP4. *Virology*, **411**, 142–152.
49. Leforestier,A. and Livolant,F. (2009) Structure of toroidal DNA collapsed inside the phage capsid. *Proc. Natl Acad. Sci. USA*, **106**, 9157–9162.
50. Cherstvy,A.G. (2011) Electrostatic interactions in biological DNA-related systems. *Phys. Chem. Chem. Phys.*, **13**, 9942–9968.
51. Schiessel,H. (2003) The physics of chromatin. *J. Phys. Condens. Matter*, **15**, R699–R774.
52. Schlick,T. (2002) *Molecular Modeling and Simulation an Interdisciplinary Guide*. Springer, New York, pp. 163–204.
53. Collepardo-Guevara,R. and Schlick,T. (2011) The effect of linker histone's nucleosome binding affinity on chromatin unfolding mechanisms. *Biophys. J.*, **101**, 1670–1680.
54. Arya,G. and Schlick,T. (2006) Role of histone tails in chromatin folding revealed by a mesoscopic oligonucleosome model. *Proc. Natl Acad. Sci. USA*, **103**, 16236–16241.
55. Arya,G., Zhang,Q. and Schlick,T. (2006) Flexible histone tails in a new mesoscopic oligonucleosome model. *Biophys. J.*, **91**, 133–150.
56. Aumann,F., Suehnel,J., Langowski,J. and Diekmann,S. (2010) Rigid assembly and Monte Carlo models of stable and unstable chromatin structures: the effect of nucleosomal spacing. *Theor. Chem. Acc.*, **125**, 217–231.
57. Wong,H., Victor,J.-M. and Mozziconacci,J. (2007) An all-atom model of the chromatin fiber containing linker histones reveals a versatile structure tuned by the nucleosomal repeat length. *Plos One*, **2**, e877.
58. Sun,J., Zhang,Q. and Schlick,T. (2005) Electrostatic mechanism of nucleosomal array folding revealed by computer simulation. *Proc. Natl Acad. Sci. USA*, **102**, 8180–8185.
59. Mergell,B., Everaers,R. and Schiessel,H. (2004) Nucleosome interactions in chromatin: fiber stiffening and hairpin formation. *Phys. Rev. E*, **70**, 011915.
60. Gay,J.G. and Berne,B.J. (1981) Modification of the overlap potential to mimic a linear site-site potential. *J. Chem. Phys.*, **74**, 3316–3319.
61. Emerson,A.P.J., Luckhurst,G.R. and Whatling,S.G. (1994) Computer-simulation studies of anisotropic systems .23. *The gay-berne discogen. Mol. Phys.*, **82**, 113–124.
62. Ambrose,C., Lowman,H., Rajadhyaksha,A., Blasquez,V. and Bina,M. (1990) Location of nucleosomes in simian virus-40 chromatin. *J. Mol. Biol.*, **214**, 875–884.
63. Ambrose,C., McLaughlin,R. and Bina,M. (1987) The flexibility and topology of simian virus-40 DNA in minichromosomes. *Nucleic Acids Res.*, **15**, 3703–3721.
64. Depken,M. and Schiessel,H. (2009) Nucleosome shape dictates chromatin fiber structure. *Biophys. J.*, **96**, 777–784.
65. Li,P.P., Nakanishi,A., Shum,D., Sun,P.C.K., Salazar,A.M., Fernandez,C.F., Chan,S.W. and Kasamatsu,H. (2001) Simian virus 40 Vp1 DNA-binding domain is functionally separable from the overlapping nuclear localization signal and is required for effective virion formation and full viability. *J. Virol.*, **75**, 7321–7329.
66. Holst,M., Baker,N. and Wang,F. (2000) Adaptive multilevel finite element solution of the poisson-boltzmann equation I. *Algorithms and examples. J. Comp. Chem.*, **21**, 1319–1342.
67. Miglioli,I., Muccioli,L., Orlandi,S., Ricci,M., Berardi,R. and Zannoni,C. (2007) A computer simulation of model discotic dimers. *Theor. Chem. Acc.*, **118**, 203–210.
68. Landau,D.P. (1976) Finite-size behavior of Ising square lattice. *Phys. Rev. B*, **13**, 2997–3011.
69. Heermann,D.W. (1986) *Computer Simulation Methods in Theoretical Physics*. Springer, Berlin, pp. 88–100.
70. Winkler,A., Wilms,D., Virnau,P. and Binder,K. (2010) Capillary condensation in cylindrical pores: Monte Carlo study of the interplay of surface and finite size effects. *J. Chem. Phys.*, **133**, 164702.
71. Huang,K. (1963) *Statistical Mechanics*. Wiley, New York, pp. 392–406.
72. Perez,M. (2005) Gibbs-Thomson effects in phase transformations. *Scr. Mater.*, **52**, 709–712.
73. Galanis,J., Nossal,R., Losert,W. and Harries,D. (2010) Nematic order in small systems: measuring the elastic and wall-anchoring constants in vibrofluidized granular rods. *Phys. Rev. Lett.*, **105**, 168001.
74. Prinsen,P. and van der Schoot,P. (2004) Continuous director-field transformation of nematic tactoids. *Euro. Phys. J. E*, **13**, 35–41.
75. Hill,T.L. (1963) *Thermodynamics of Small Systems*. W.A. Benjamin, New York, pp. 89–132.
76. Fritsche,M., Li,S.L., Heermann,D.W. and Wiggins,P.A. (2012) A model for *Escherichia coli* chromosome packaging supports transcription factor-induced DNA domain formation. *Nucleic Acids Res.*, **40**, 972–980.
77. Bradford,M.M. (1976) Rapid and sensitive method for quantitation of microgram quantities of protein utilizing principle of protein-dye binding. *Anal. Biochem.*, **72**, 248–254.

78. Rosenberg,B.H., Deutsch,J.F. and Ungers,G.E. (1981) Growth and purification of Sv40 virus for biochemical-studies. *J. Virol. Methods*, **3**, 167–176.
79. Schachman,H.K. (1957) In: Colowick,S.P. and Kaplan,N.O. (eds), *Methods in Enzymology*, Vol. IV. Academic Press Inc., New York, pp. 125–204.
80. Laemmli,U.K. (1970) Cleavage of structural proteins during assembly of head of bacteriophage-T4. *Nature*, **227**, 680–685.
81. Sandalon,Z. and Oppenheim,A. (1997) Self-assembly and protein-protein interactions between the SV40 capsid proteins produced in insect cells. *Virology*, **237**, 414–421.
82. Pace,C.N., Vajdos,F., Fee,L., Grimsley,G. and Gray,T. (1995) How to measure and predict the molar absorption-coefficient of a protein. *Protein Sci.*, **4**, 2411–2423.
83. Hammersley,A.P., Svensson,S.O., Hanfland,M., Fitch,A.N. and Hausermann,D. (1996) Two-dimensional detector software: from real detector to idealised image or two-theta scan. *High Press. Res.*, **14**, 235–248.
84. Luckhurst,G.R. and Simmonds,P.S.J. (1993) Computer-simulation studies of anisotropic systems .21. Parametrization of the gay-berne potential for model mesogens. Mol. Phys., **80**, 233–252.
85. Livolant,F. and Leforestier,A. (2000) Chiral discotic columnar germs of nucleosome core particles. *Biophys. J.*, **78**, 2716–2729.
86. Leforestier,A., Dubochet,J. and Livolant,F. (2001) Bilayers of nucleosome core particles. *Biophys. J.*, **81**, 2414–2421.
87. Dolinsky,T.J., Czodrowski,P., Li,H., Nielsen,J.E., Jensen,J.H., Klebe,G. and Baker,N.A. (2007) PDB2PQR: expanding and upgrading automated preparation of biomolecular structures for molecular simulations. *Nucleic Acids Res.*, **35**, W522–W525.
88. Dolinsky,T.J., Nielsen,J.E., McCammon,J.A. and Baker,N.A. (2004) PDB2PQR: an automated pipeline for the setup of Poisson-Boltzmann electrostatics calculations. *Nucleic Acids Res.*, **32**, W665–W667.
89. West,B., Brown,F.L.H. and Schmid,F. (2009) Membrane-protein interactions in a generic coarse-grained model for lipid bilayers. *Biophys. J.*, **96**, 101–115.
90. Low,R.J. (2002) Measuring order and biaxiality. *Eur. J. Phys.*, **23**, 111–117.